Erosive granular avalanches: a cross confrontation between theory and experiment

Eric Clément · Florent Malloggi · Bruno Andreotti ·
Igor S. Aranson

Abstract Results on two laboratory scale avalanches experiments taking place both in the air and under-water, are presented. In both cases a family of solitary erosion/deposition waves are observed. At higher inclination angles, we show the existence of a long wavelength transverse instability followed by a coarsening and the onset of a fingering pattern. While the experiments strongly differ by the spatial and time scales, the agreement between the stability diagram, the wavelengths selection and the avalanche morphology suggest a common erosion/deposition scenario. These experiments are studied theoretically in the framework of the "partial fluidization" model of dense granular flows. This model identifies a family of propagating solitary waves displaying a behavior similar to the experimental observation. A primary cause for the transverse instability is related to the dependence of avalanche velocity on the granular mass trapped by the flow.

E. Clément (✉) · F. Malloggi · B. Andreotti
ESPCI-Universités Paris 6 and 7,
Laboratoire de Physique et Mécanique des Milieux Hétérogénes,
UMR7636, 10, rue Vauquelin, 75005 Paris, France
e-mail: erc@ccr.jussieu.fr

B. Andreotti
e-mail: andreotti@pmmh.espci.fr

Present Address:
F. Malloggi
Physics of Complex Fluids University of Twente,
PO Box 217, 7500 AE Enschede, The Netherlands
e-mail: F.G.J.Malloggi@tnw.utwente.nl

I. S. Aranson
Materials Science Division, Argonne National Laboratory,
9700 South Cass Avenue, Argonne, IL 60439, USA
e-mail: aronson@msd.anl.gov

1 Introduction

Avalanching processes leading to catastrophic transport of various natural materials do not only occur in the air as we know of snow avalanches, mud flows, land slides. Such events frequently happen below the see level as they take many forms from turbidity currents to thick sediment waves sliding down the continental shelf. From the risk assessment point of view, important issue is evaluation to which extend an initial triggering event (an earth quake or an eruption) would be responsible for a subsequent process that might propagate or amplify over large distances as an unstable matter wave. Unfortunately, the dynamics of such catastrophic events so far lacks a conceptual clarity [1,2] since (i) the rheology of the flows involved in an avalanche is complex and still not unraveled; (ii) the physics of erosion/deposition mechanisms is essentially limited to empirical descriptions based on dimensional analysis and semi-empirical formulations. There were several theoretical attempts to describe from a phenomenological point of view the dynamics of erosion waves as an interplay between a rolling phase and a static phase [3,4]. While extensive laboratory-scale experiments on dry and submerged granular materials flowing on rough inclined plane [5–7] have brought new perspectives for the elaboration of reliable constitutive relations, many aspects of avalanches propagation on erodible substrates still are not understood [8–14]. It has been shown experimentally that families of localized triangular shape avalanches can be triggered in the metastability domain, between the stoppage angle and maximal avalanche angle. [8]. Also, the shape

of other localized droplet-like waves was recently shown to depend strongly on the intimate nature of the granular material [11]. All these issues are closely related to the compelling need for reliable description of the fluid/solid transition for particulate assemblies in the vicinity of the flow arrest. Here, we present experimental results concerning avalanche fronts developing over an erodible granular substrate, both in the air and under water. The avalanche fronts flowing on solid rough substrates (non-erodible) are transversally stable: the transverse coupling due to gravity being essentially a stabilizing mechanism [5,15]. But, when a segregation occurs, an avalanche front on a rough substrate may exhibit a fingering pattern explained by a pinning mechanism [16,17]. Since the rough grains we used in experiment have a narrow polydispersity (25%), we investigate here a quite different mechanism. We demonstrate the existence of a linear transverse instability of the solitary front occurring at higher inclination angles.

A model of "partially fluidized" dense granular flows was developed to couple a phenomenological description of a solid/fluid transition with hydrodynamic transport equations. It reproduces many features found experimentally such as metastability of a granular deposits, triangular down-hill and balloon-type up-hill avalanches and variety of shear flow instabilities [9,10,18]. The model was later calibrated with molecular dynamics simulations [19]. Here the partial fluidization model is applied to solitary avalanches flowing over a thin erodible sediment layer. A set of equations describing the dynamics of fully eroding waves is derived and a family of solitary wave solutions propagating downhill is obtained. The velocity and shape selection of these waves is investigated as well as the existence of a linear transverse instability. The primary cause for the transverse instability is associated with the dependence of the solitary avalanche velocity with the mass trapped in the flow. A numerical study is conducted to follow the nonlinear evolution of the avalanche front. The results are discussed in the context of experimental findings [12–14].

2 Experiments on erosion waves

Description of the setups. The experimental setups consist of a thin granular layer deposited on an incline plane (chute) that can be tilted at a value θ (Fig. 1a). The "dry" setup is similar to the one of Daerr et al. [8,20]. The size of the chute is 70 cm wide and 120 cm long. The granular medium is either Fontainebleau sand; typical size $d = 300 \pm 60$, or 500μm monodisperse glass beads. The chute bottom is made of black velvet. For the under water avalanches, the setup size is smaller: the chute width is 15 cm and so is the length. The granular sediment is an aluminum oxide powder of size either $d = 30$ or 40 ± 11 μm. To avoid inter-particle cohesion, the
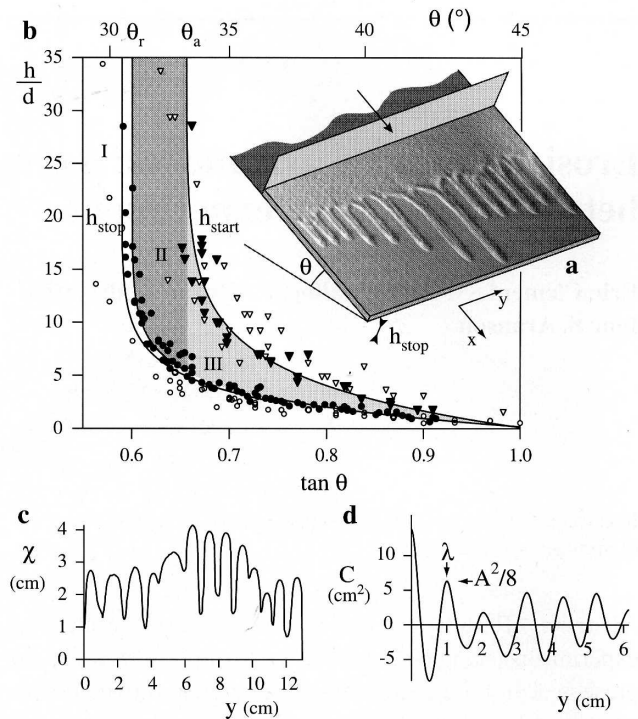
Fig. 1 a Experimental setup. **b** Stability diagram: h_{stop} is the thickness of the sediment left after an avalanche for a given angle θ, in air, sand (*filled circle*) and in water (*open circle*); $h_{start}(\theta)$ is the maximum stable height of sediment, in air (*inverted filled triangle*) and in water (*inverted open triangle*). $h_{start}(\theta)$ and $h_{stop}(\theta)$ are fitted by the form $h = b \log((\tan \theta - \mu)/\delta\mu)$ (*solid lines*). In region I, an avalanche front cannot propagate autonomously down the slope: the perturbations fade away when the driving stops. Avalanches triggered in region II are stable while they exhibit a transverse instability in region III. In particular, solitary erosion waves are observed when starting from the stable height h_{stop}. **c** Front profile $\chi(y)$ obtained from image processing. **d** The corresponding correlation function $C(y)$ allows defining the average wavelength λ and the amplitude A_m

pH value is maintained close to 4 by adequate addition of hydrochloric acid [21]. The chute is initially set at an horizontal position and a fixed mass of powder is poured and suspended by vigorous stirring. A uniform sediment layer of height h then forms within 10 min. The bottom is an abraded but transparent plexiglass plate which offers the possibility to monitor the avalanche dynamics by transparency when illuminated from below. The profile of the avalanche front $h(x, t)$ is obtained with a laser slicing technique and is resolved within 30 μm (0.1 d) in the dry case. The front dynamics is quantitatively monitored by image processing of the avalanche front pictures. The front line position $\chi(y, t)$ is then extracted (Fig. 1c) and the front line autocorrelation function $C(y, t) = \langle \chi(y + y', t)\chi(y', t)\rangle_{y'}$ is computed. Then, the correlation function's first maximum is identified from which the average wavelength λ and the amplitude $A_m = \sqrt{8C(\lambda)}$ are extracted, see Fig. 1d. In addition, the surface velocity

field is measured by a Particle Image Velocimetry technique for dry avalanches.

The sand layer stability diagrams. It has been shown that the stability of dry granular layers of depth h lying on a flat substrate inclined at an angle θ can be described by a diagram with two critical curves [5]: $h_{start}(\theta)$ and $h_{stop}(\theta)$, see Fig. 1b. The curves have the following interpretation: a uniform deposit of height h will globally loose its stability if tilted above the angle θ defined by $h = h_{start}(\theta)$ and the avalanching process will leave at rest a deposit of height $h_{stop}(\theta)$. h_{start} and h_{stop} curves diverge at two different asymptotic angles, respectively, equal to the avalanche angle of the granular pile θ_a and to the repose angle θ_r. Between these two curves, a domain of metastability for the granular deposit is present. $h_{start,stop}$ curves obtained for dry and underwater layers bear the same features and fall on the same curve when the deposited height is rescaled by d, see Fig. 1b.

Solitary erosion/deposition waves. To initiate avalanche fronts both in air and under water, we designed a "bulldozer" technique: a plate perpendicular to the avalanche track scrapes the sediment at a constant velocity (Fig. 1a). While our results on avalanche stability are valid in the whole metastable region (Fig. 1b), we will limit ourselves to the experiments started from a stable sediment layer of height $h_{stop}(\theta)$. Once an autonomous avalanche front separates from the plate, the bulldozer driving stops. For $\theta_r < \theta < \theta_a$, we always obtain transversely stable avalanche fronts, both in wet and dry cases. We observed that the avalanche quickly converges toward an asymptotic form. For this systematic study, we have kept a constant scraping velocity at about one-third of the typical avalanche velocity v_a and deposited the minimal mass required to trigger a solitary wave. Then, under these conditions the solitary wave is found to be rather insensitive to the preparation details within a range of scraping velocities. For this systematic study, we have kept a constant scraping velocity at about one-third of the typical avalanche velocity v_a. In the water, v_a is of the order of the Stokes velocity $\frac{\Delta\rho}{\rho_w}\frac{gd^2}{18\,v_w} \simeq 2$ mm/s where $\Delta\rho/\rho_w = 3$ is the density contrast between grains and water, v_w the water kinematic viscosity and g the gravity acceleration. In the air, the propagation velocity is of the order of $\sqrt{gd} \simeq 5$ cm/s. Figure 2 shows the sediment height h and the surface velocity v profiles for such an avalanche.

The transverse instability. In the case of rough sand particles, the autonomous wave fronts are transversally unstable for $\theta > \theta_a$. However, no transverse instability was observed for smooth monodisperse glass beads. It is worth noticing that for the same angles, avalanches down a solid rough plate are stable (at least in the dry case). After the initial instability,
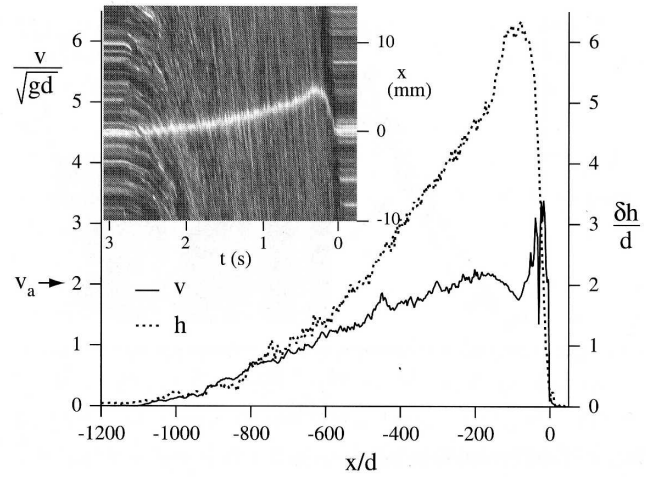

Fig. 2 Solitary erosion wave profile $\delta h = h - h_{stop}$ rescaled by d (*dotted line*) and surface velocity profile v rescaled by $\sqrt{gd}$ (*solid line*) (dry sand, $\theta = 32°$, $h_{stop} = 2.3$ mm $= 7.8$ d, region II). *Inset* spatio-temporal diagram done with a fast camera (125 Hz), showing the particle motion as well as the profile height (deflection of the laser sheet). It is observed that the surface grain velocity at the front tends towards the solitary wave velocity v_a ($v_a \approx 2\sqrt{gd}$ for given experimental conditions)
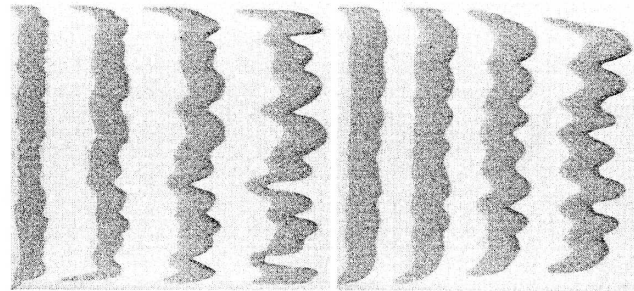

Fig. 3 Flowing part of solitary waves visualized by image difference (air, sand, $d = 300$ μm, $\theta = 35°$, time interval 1.1 s), starting from a flat bed (*left*) or from an initial bed presenting a forced wavelength $\lambda = 6.5$ cm

we have identified a coarsening scenario responsible for a sequence of fusion processes increasing the spatial modulation lengths. Finally, the transverse destabilization ends up as a fingering pattern. In this final stage, the flowing zones are disconnected one from the others so that the wavelength does not evolve. Figure 4 displays a typical time evolution of the dominant wavelength extracted from the correlation function. In inset, a typical fusion event illustrates the coarsening scenario. Because of the competition between unstable modes and the coarsening process, the identification of a generic scenario for the transverse instability is technically difficult.

In addition to the experiments started from a flat bed described above, we performed series of experiments starting from a modulated initial condition. The modulation at a given wavelength is simply produced by imprinting on the
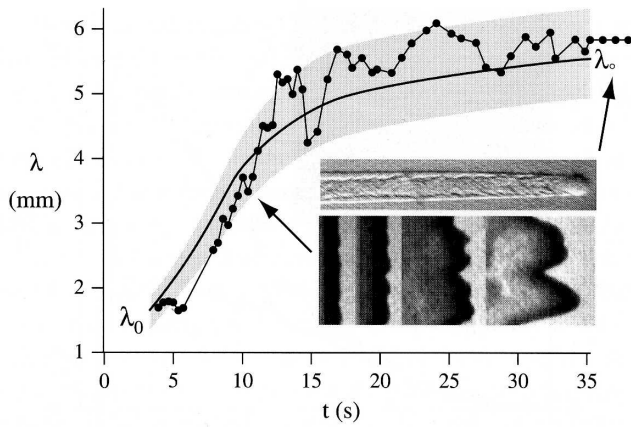
Fig. 4 Time evolution of the wavelength λ (water, $d = 40$ μm, $\theta = 37.1°$) in a typical realization (*filled circle*) and averaged over many realizations (*solid line*, the *shadow zone* indicates the standard deviation). After a small plateau at the initial wavelength λ_0, λ increases due to coalescence processes (*lower photograph*) until it reaches the value λ_∞ corresponding to formation of non-interacting fingers (*upper photograph*)
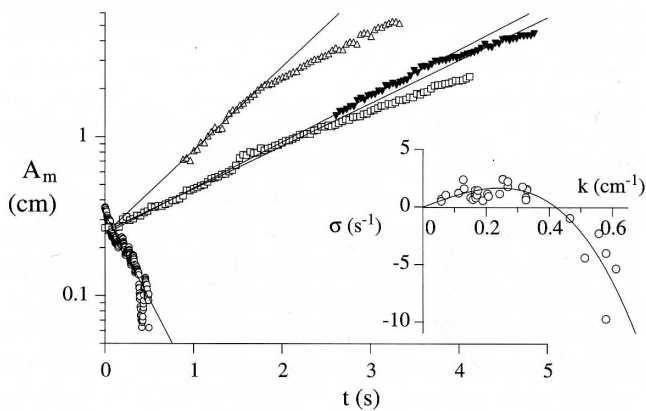
Fig. 5 Time evolution of the amplitude A_m (air,sand $d = 300$ μm, $\theta = 35°$) for initial condition forced at the wavelength $\lambda = 12$ mm (*open circle*), $\lambda = 30$ mm (*open square*), $\lambda = 90$ mm (*triangle*) and $\lambda = 178$ mm (filled triangles). *Inset* linear growth rate σ as a function of the wave number k. The *solid line* is the best fit by $\sigma = a|k| - bk^2$, with a maximum growth rate $\sigma_m \simeq 2.5$ s^{-1} for $\lambda_0 \simeq 4$ cm. Measurement of λ_0 from an undisturbed solitary wave (Fig. 3) gives 3.3 cm

sediment surface regularly spaced thin scarification (shallow scratches). We have found that the forced modes always fade away in region II. On the other hand, in region III the front modulation amplifies exponentially for a wide band of wavelengths. The linear regime is clearly evidenced over one decade in amplitude. Nonlinear effects start being visible when the amplitude becomes of the order of 1 cm. The inset to Fig. 5 shows the dispersion relationship deduced from these measurements confirming a long wavelength linear instability.

For experiments both in the air and in the water, performed in the unstable regime, we extracted two characteristic wavelengths. The initial wavelength λ_0 would correspond, to the
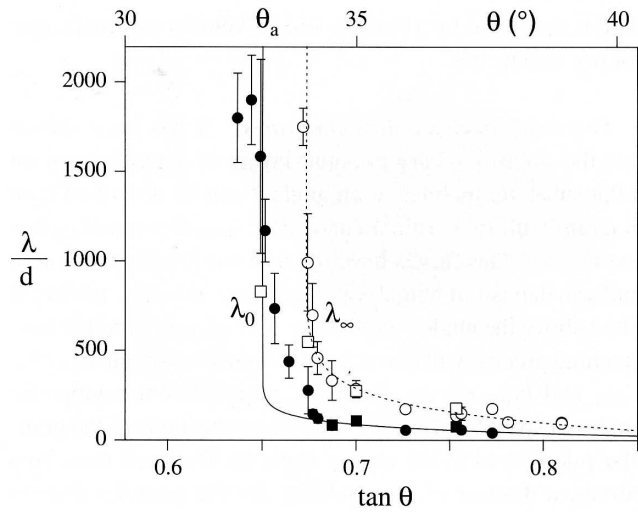
Fig. 6 Initial (*filled circle*) and final (*open circle*) wavelengths rescaled by d as a function of θ ($d = 40$ μm, in water). The initial wavelength data in air (*filled square*) and water (*filled circle*) coincide, as well as the final wavelength data in air, sand (*open square*) and water (*open circle*). The *error bars* correspond to the dispersion of the data from a realization to the other. As λ_0 diverges at θ_a, we have superimposed the curve $10 \times h_{start}(\theta)$ (*solid line*), which is a good approximation of λ_0 to some extent. The *dotted line* is the best fit of the final wavelength λ_∞ by the same logarithmic law similar to $h_{start}(\theta)$ or $h_{stop}(\theta)$

best of our experimental possibilities, to the fastest growing linear mode. Then, the larger wavelength λ_∞ is measure at the onset of the fingering instability. Figure 6 displays both wavelengths rescaled by the grains sizes: λ_0/d and λ_∞/d, versus the inclination angle θ. The selected wavelengths are typically larger than a grain size by at least two orders of magnitude.[1] Constrained by finite size effects and measurements uncertainties, we obtain that the value $\theta \cong \theta_a$ corresponds to a diverging boundary for the initial wavelength λ_0/d. This is a signature of a zero wave-number instability with a threshold close to θ_a. Another striking feature is the collapse, *on the same curve*, of the data obtained in the air and underwater, once rescaled by the grain size. In the range of parameters where the fingering regime is reached before the end of the chute, the ratio of the final to the initial wavelength is approximately constant and close to $\lambda_\infty/\lambda_0 \simeq 3.5$. The presence of a fingering is a quite fascinating feature of this avalanching process. The fingering front stems from the onset of localized propagating waves following the transverse instability regime. These fingers are localized matter droplets with levees on the side. They evolve into a quasi solitary mode when they are fully developed; their selected width is found to be quite sensitive to the slope ($\simeq \lambda_0$ for both wet and dry cases).

---

[1] Note that the largest wavelengths measured are of the order of the chute width (1,800 d in water and 750 d in air).

3 The partial fluidization model

We apply the *partial fluidization model* to investigate the avalanche dynamics on a thin erodible sediment layer. According to the partial fluidization theory [9,10], the ratio of the static part of the shear stress σ^s to the fluid part σ^f of the full stress tensor σ is controlled by an order parameter (OP) ρ, $\sigma^f = Q(\rho)\sigma$; $\sigma^s = (1 - Q(\rho))\sigma$, where the OP ρ is scaled in such a way that in granular solid $\rho = 1$ and in the fully developed flow (granular liquid) $\rho \to 0$. Correspondingly, the function $Q(\rho)$ satisfies the following conditions $Q \to 0$ for $\rho \to 1$ and $Q \to 1$ for $\rho \to 0$. The simplest choice $Q = 1 - \rho$ appears to be in a good agreement with soft particles simulations [19]. The fluid stress σ^f is assumed to be of the form

$$\sigma_{ij}^f = \nu(\partial_j v_i + \partial_i v_j), \quad i \neq j \tag{1}$$

where v_i is the velocity component and ν is the granular shear viscosity. The full stress σ can be obtained, for example, from the static equilibrium conditions.

At the "microscopic level", the OP is defined as a fraction of the number of persistent particle contacts to the total number of contacts. Due to a strong dissipation in dense granular flows, ρ is assumed to obey purely relaxational dynamics controlled by the Ginzburg-Landau equation for generic first order phase transition,

$$\tau_\rho \frac{D\rho}{Dt} = l_\rho^2 \nabla^2 \rho - \frac{\partial F(\rho, \delta)}{\partial \rho}. \tag{2}$$

Here $\tau_\rho, l_\rho \approx d$ are the OP characteristic time and length scales, d is the grain size. $F(\rho, \delta)$ is a free energy density which is postulated to have two local minima at $\rho = 1$ (solid phase) and $\rho = 0$ (fluid phase) to account for the bistability near the solid–fluid transition. The relative stability of the two phases is controlled by the parameter δ which in turn is determined by the stress tensor σ_{nm}. The simplest assumption consistent with the Mohr-Coulomb yield criterion is to take it as a function of $\phi = \max|\sigma_{mn}/\sigma_{nn}|$, where the maximum is sought over all possible orthogonal directions m and n.

For thin layers Eq. (2) can be simplified by fixing the structure of the OP in z-direction (z perpendicular to the bottom, x is directed down the chute and y in the vorticity direction): $\rho = 1 - A(x, y)\sin(\pi z/2h)$, h is the local layer thickness, A is slowly-varying function. This approximation valid for thin layers when there is no formation of static layer beneath the avalanche (see below). Then one obtains equations governing the evolution h and A (coordinates x, y, height h, and time t are normalized by l_ρ, τ_ρ correspondingly [9,10,14,18]),

$$\frac{\partial h}{\partial t} = -\alpha \frac{\partial h^3 A}{\partial x} + \frac{\alpha}{\phi} \nabla \left(h^3 A \nabla h\right) \tag{3}$$

$$\frac{\partial A}{\partial t} = \Lambda_0 A + \nabla^2 A + \frac{8(2 - \delta)}{3\pi} A^2 - \frac{3}{4} A^3 \tag{4}$$

where $\nabla^2 = \partial_x^2 + \partial_y^2$, $\Lambda_0 = \delta - 1 - \pi^2/4h^2$, dimensionless transport coefficient:

$$\alpha \approx \frac{2(\pi^2 - 8)}{\pi^3 \nu} g \tau_\rho l_\rho \sin\theta, \tag{5}$$

where $\phi = \tan\theta$. Control parameter δ assumes the form $\delta(\tilde{\theta}) = ((\tan\tilde{\theta})^2 - \phi_0^2)/(\phi_1^2 - \phi_0^2)$, $\phi_{0,1}$ are tangents of dynamic and static repose angles respectively, θ_r and θ_a. Correspondingly, $\tan\tilde{\theta}$ is the local slope of granular layer. Assuming that the slope of the layers $\tan\tilde{\theta}$ is close to the chute slope $\tan\theta$, we can expand the control parameter $\delta \approx \delta_0 + \beta h_x$, $\delta_0 = \delta(\theta)$, $\beta \approx 1.5 - 3$ depending on the value of θ, see for detail [9,10,14,18]. The last term in Eq. (3) is also due to change of local slope and is obtained from expansion $\tilde{\theta} = \theta + h_x$. This term is responsible for the saturation of the slope of avalanche front (without it the front can be arbitrary steep) [14,18].

Solitary wave shape selection. In the frame co-moving with the velocity V, Eqs. (3),(4) assume the form

$$\frac{\partial h}{\partial t} = V \partial_x h - \alpha \frac{\partial h^3 A}{\partial x} + \frac{\alpha}{\phi} \nabla \left(h^3 A \nabla h\right) \tag{6}$$

$$\frac{\partial A}{\partial t} = V \partial_x A + \Lambda_0 A + \nabla^2 A + \frac{8(2 - \delta)}{3\pi} A^2 - \frac{3}{4} A^3 \tag{7}$$

Numerical studies revealed that the one-dimensional Eqs. (6), (7) possess a one-parametric family of localized (solitary) solutions, see Fig 7:

$$A(x, t) = A(x - Vt), \quad h(x, t) = h(x - Vt) \tag{8}$$

Here the boundary conditions take a form $h \to h_0$, $A \to 0$ for $x \to \pm\infty$, where h_0 is the asymptotic height. The one-dimensional steady-state solution (8) satisfy
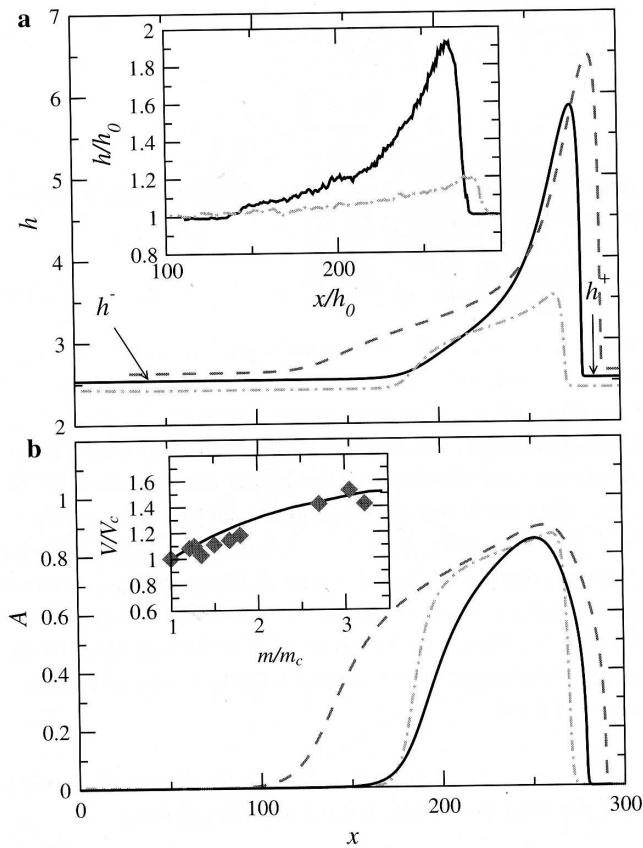
$$V(h - h_0) = \alpha h^3 A \left(1 - \frac{\partial_x h}{\phi}\right) \tag{9}$$

$$-V \frac{\partial A}{\partial x} = \Lambda_0 A + \partial_x^2 A + \frac{8(2 - \delta)}{3\pi} A^2 - \frac{3}{4} A^3 \tag{10}$$

The solutions can be parameterized by the "trapped mass" m carried by the wave, i.e. the area above h_0,

$$m = \int_{-\infty}^{\infty} (h - h_0) dx \tag{11}$$

The velocity V is increasing function of m, see inset to Fig. 7a. The family of admissible solutions for a propagative solitary wave terminates at $m = m_c$ and $V = V_c = V(m_c)$.

Fig. 7 Height h (**a**) and fluidization parameter A (**b**) for various values of avalanche mass m and transport coefficient α. *Solid line* is for $m = 147.7$, $V = 2.72$, *dashed line* is for $m = 211$, $V = 3.12$, for $\delta = 1$, $\alpha = 0.08$, $\beta = 2$; *point-dashed line* is for $\alpha = 0.025$, $\delta = 1.15$, $m = 62$, $V = 0.86$. Inset to Fig. 7a: Representative height profiles for avalanches in sand (*solid line*) and glass beads (*dashed line*). *Inset* to **b**: Avalanche velocity V vs. m (*solid line*), diamonds depict experimental data for sand avalanches

The critical mass m_c decreases with the increase in α. The dependence of V vs. m is (qualitatively) consistent with experimental data, see inset to Fig. 7b for sandy avalanches in the air. Note that this experimental curve was obtained by collecting the falling sand at the end of the avalanche plane when erosion waves of different sizes were triggered. We also notice that below a mass threshold, no propagation of an erosive wave is possible. The structure of the solutions is sensitive to the value of α: for large α the solution has a well-pronounced shock-wave shape, Fig. 7a, with the height of the crest $h_{\max}$ several times larger than the asymptotic depth h_0. For $\alpha \to 0$ the solution assumes more rectangular form, see Fig. 7b, and $h_{\max} - h_0 \ll h_0$. The results are consistent with the shape of sand (compare with large α) and glass bead ($\alpha \to 0$) avalanches, see inset to Fig. 7a

The front linear transverse instability. To understand transverse instability we focus on the solitary solution with slowly varying position $x_0(y, t)$

$$A(x, t) = \bar{A}(x - x_0(t, y)), \quad h(x, t) = \bar{h}(x - x_0(t, y))$$
$$(12)$$

Substituting Eq. (12) in Eq. (6) and integrating over x, one obtains

$$\partial_t m = V(m)(h^+ - h^-(m)) - \zeta_1 \partial_y^2 x_0 + \zeta_2 \partial_y^2 m \qquad (13)$$

where $\zeta_{1,2} = const$ is defined as

$$\zeta_1 = \frac{\alpha}{\phi} \int_{-\infty}^{\infty} \left(\bar{A} \bar{h}^3 \partial_x \bar{h} \right) dx, \quad \zeta_2 = \frac{\alpha}{\phi} \int_{-\infty}^{\infty} \left(\bar{A} \bar{h}^3 \partial_m \bar{h} \right) dx$$

Here $h^+ = h(x \to \infty)$ is the height of the deposit layer ahead of the front and $h^- = h(x \to -\infty)$ is the height behind the front, see Fig. 7a. While the value of h^+ is prescribed by the initial sediment height, the value of h^- behind the front is determined by the velocity (or mass) of the front. For steady-state solution $h^+ = h^- = h_0$. For the slowly-evolving solution the difference between h^+ and h^- can be small, however it is important for the stability analysis. These terms are also necessary to describe the experimentally observed initial acceleration/slowdown of the avalanches. Substituting Eqs. (12) into Eq. (4) and performing orthogonality conditions one obtains[2]

$$\partial_t x_0 = V(m) + \partial_y^2 x_0 \qquad (14)$$

To see the onset of the instability we keep only the leading terms in Eqs. (13), (14), using expansions $V(m) \approx V(m_0) + V_m(m - m_0)$, and $\tilde{m} = m - m_0 \ll m_0$:

$$\partial_t \tilde{m} = -\tau \tilde{m} - \zeta_1 \partial_y^2 x_0 + \zeta_2 \partial_y^2 \tilde{m}; \quad \partial_t x_0 = V_m \tilde{m} + \partial_y^2 x_0$$
$$(15)$$

where $m_0 = const$ is the steady-state mass of the solitary wave, and $\tau = V(m_0)\partial_m h^-$. Seeking solution in the form $m, x_0 \sim \exp[\sigma t + iqy]$, q is the transverse modulation wave-number, for the most unstable mode we obtain from Eq. (15) the growthrate σ

$$\sigma = \frac{-q^2(1 + \zeta_2) - \tau + \sqrt{(q^2(1 - \zeta_2) - \tau)^2 + 4V_m \zeta_1 q^2}}{2}$$
$$(16)$$

Expanding Eq. (16) for $q \to 0$ we obtain $\sigma \approx \frac{1}{2}(2V_m\zeta_1/\tau - 1)q^2 + O(q^4)$. The instability occurs if $V_m\zeta_1/\tau - 1/2 > 0$. Substituting τ and using $V_m/h_m = V_h$, we obtain a simple instability criterion $2V_h\zeta_1/V > 1$ giving a value of threshold α since $\zeta_1 \sim \alpha$. For $\alpha < \alpha_c$ no instability occurs, and the modulation wavelength diverges for $\alpha \to \alpha_c$. Far away from the threshold we neglect τ and then obtain for $\sigma(q)$:

[2] There are also higher order terms in Eq. (14) which we neglect for simplicity.
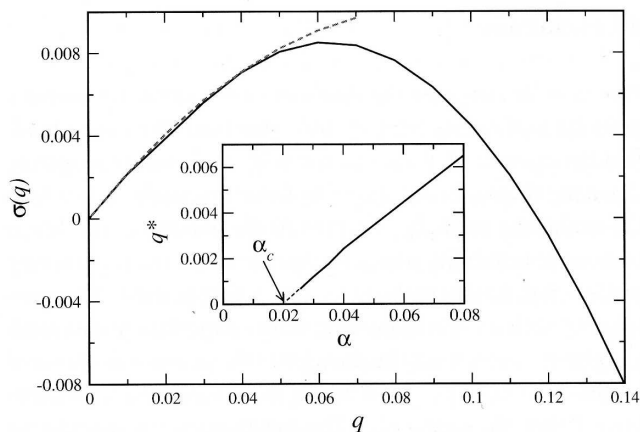
Fig. 8 Growthrate $\sigma(q)$ vs. q for $\delta = 1.15$ and $\alpha = 0.08$ for the mass of the avalanche $m = 102$. *Solid line* $\sigma(q)$ obtained by numerical stability analysis of one-dimensional solution Eq. (12). *Dashed line* is solution of Eq. (16). *Inset* optimal wavenumber of q^* vs. α for $\delta = 1.15$

$$\sigma = |q|\sqrt{\zeta_1 V_m} - (1 + \zeta_2)q^2/2 + O(q^3) \qquad (17)$$

The optimal wavenumber q^* is given by $q^* \sim \sqrt{\zeta_1 V_m} \sim \alpha$.

Figure 8 shows $\sigma(q)$ obtained by numerical stability analysis of linearized Eqs. (3), (4) near the one-dimensional solution Eq. (8). For comparison the solution to Eq. (16) is shown, with the parameters extracted from the corresponding one-dimensional steady-state problem Eqs. (9), (10). One sees that Eq. (16) gives correct description for small q, however fails to predict $\sigma(q)$ in the whole range of q. For this purpose one needs to include higher order terms. Thus, Eq. (16) gives correct description of the onset of instability and qualitative estimate for the selected wavenumber q^*. Inset to Fig. 8 shows the dependence of optimal wavenumber q^* vs α, obtained by numerical linear stability analysis of the solitary solution. It shows almost linear decrease of q^* with α consistent with prediction. For very small α the plot indicates that $q^* \to 0$ at $\alpha \to \alpha_c$, consistent with Eq. (17). From the qualitative point of view, the transverse instability of planar front is caused by the following mechanism: local increase of solitary wave mass results in the increase of its velocity and, consequently, "bulging" of the front. Since the bulge "rolls" forward, i.e below the level of the avalanche, the granular fluid flows towards the bulge, further draining the trailing regions.

Coarsening and fingering. To study avalanche fronts beyond the initial linear instability, a fully two-dimensional numerical analysis of Eqs. (3), (4) was performed. Integration was carried out in a rectangular domain with periodic boundary conditions in x and y directions. Number of mesh points was up to $1{,}200 \times 600$ or higher. As an initial condition we used a flat state $h = h_0$ with a narrow stipe $h = h_0 + 2$ deposited along the y-direction. To trigger the
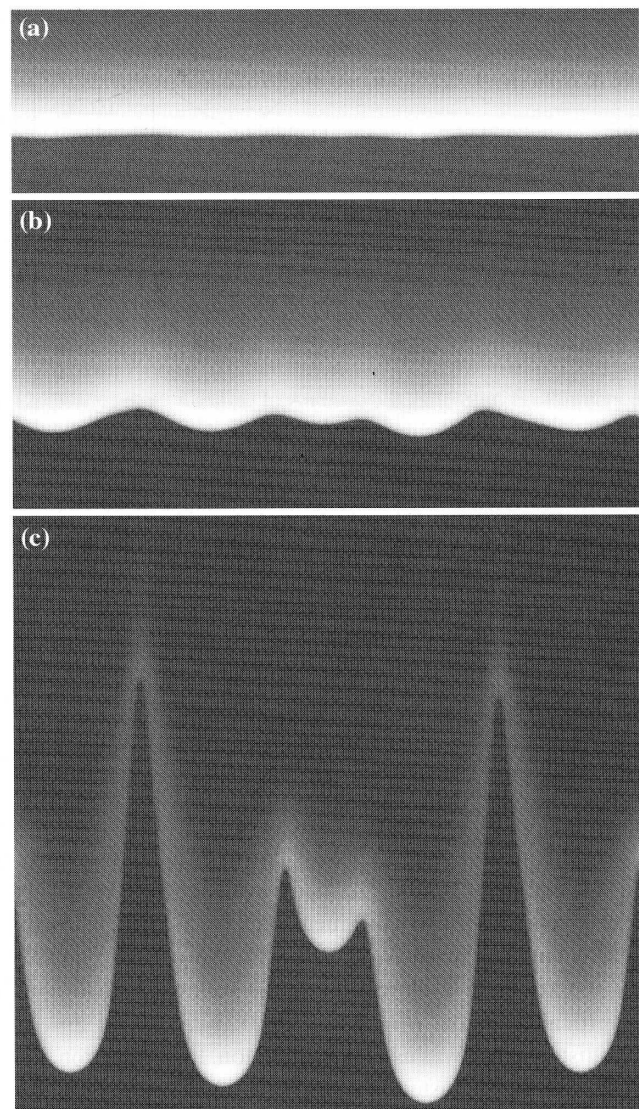
Fig. 9 Grey-coded images of height profile $h(x, y)$ (white corresponds to larger height) for three different moments of time, **a** $t = 170$, **b** $t = 300$ and **c** $t = 500$ units of time. Domain size is 600 units in x direction and 450 units in y direction, only part of domain in x direction is shown. Parameters: $\delta = 1.16$, $\alpha = 0.14$, $\beta = 2$ and initial height $h_0 = 2.285$

transverse instability, a small noise was added to the initial condition. The initial condition rapidly developed into a quasi-one-dimensional solution described by Eq. (8). Due to the periodicity in the x-direction, the solitary solution could pass through the integration domain several times. It allowed us performing analysis in a relatively small domain in the x-direction. The transverse modulation of the solitary wave leading front was observed after about 100 units of time for the parameters of Fig. 9. We observe that modulation initially grows in amplitude, eventually coarsens and leads to the formation of large-scale finger structures.
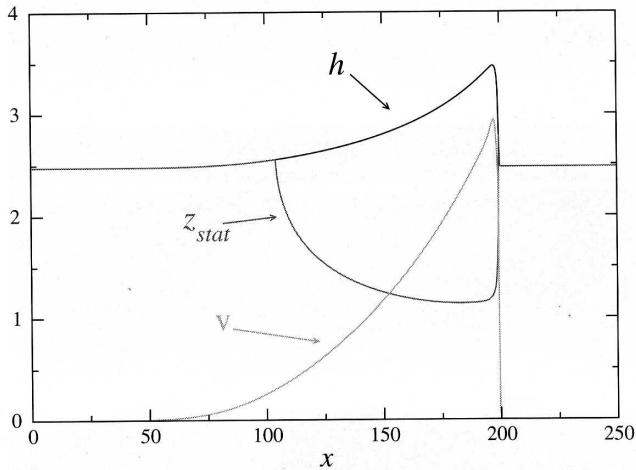
Fig. 10 Representative height h, the static layer depth z_{stat} and the top surface velocity $v(x)$ profiles for solitary avalanche for $\delta_0 = 0.729$, $h_0 = 2.6$ which is close to h_{stop}

Solitary avalanches in deep layers. The method of solution to Eq. (2) described above is applicable to relatively thin layers when the vertical profile of the OP can be approximated by $\rho = 1 - A(x, y)\sin(\pi z/2h)$. In deep granular layers this approximation breaks down, and, consequently, Eq. (4) becomes invalid. To study avalanches in relatively thick layers we solved two-dimensional (x, z) Eq. (2) directly in a rectangular mesh $N_x \times N_z$, with the periodic boundary conditions in x-direction and the following conditions in vertical direction: $\rho = 1$ for $z = 0$, $\partial_z \rho = 0$ for $z = h$. Equidistant mesh was used in x-direction. In z-direction, the mesh size was adjusted to h, $dz = h(x)/N_z$. The height h was obtained from the mass conservation law, $\partial_t h = -\partial_x J$, where the total grain flux is $J = \int_0^h v(x, z)dz$, $v(x, z)$ is the hydrodynamic velocity obtained from integration of constitutive relation (1). We also took into account that in the deep layers the viscosity ν is the function of hydrostatic pressure p, i.e depends on z-coordinate as $\nu \sim \sqrt{h - z}$ (the details will be published elsewhere). We used $N_x = 600$, $N_z = 50$, length in x-direction $L = 250$. Representative results are shown in Fig. 10. As an initial condition we choose localized bump. After short transient the bump develops into a localized avalanche traveling with a constant speed. The shape of the avalanche and the surface velocity profile are similar to the experimental observations, compare with Fig. 2. From the numerical results we were able also to obtain the depth of static layer beneath the moving avalanche, z_{stat}. The value of z_{stat} was extracted from the condition $v(z = z_{stat}) = 0.1 v(z = h)$. As one sees from the figure, only a small fraction of the sand is fluidized ($z_{stat} < z < h$) in the course of avalanche propagation, the rest of the material is in the static state.

4 Conclusions

We have investigated the dynamics of underwater and dry granular avalanches on a erodible substrate. We have identified the domain of existence for solitary waves propagating down the slope without changing form. For angles larger than the avalanche angle θ_a, we proved the existence of a linear transverse instability which further develops via a coarsening process and finally ends up as a fingering pattern. The existence of solitary waves provide a new important test to models. For instance, it may be shown that they cannot be captured by Saint-Venant-type models not including a static erodible layer below the avalanche. The mechanism responsible for the instability reminiscent of a standard zero wave number instability at threshold θ_a. The inhibition of this instability on a solid bottom suggests that erosion/deposition processes in the avalanche depth could play a crucial role. Further studies with other materials on different substrates are needed to determine the robustness of instability scenario. A challenging experimental issue is obtaining a more focused vision on the interface separating the jammed and the rolling phases, and its relation to the instability onset. In the final stage of the instability, the fingers appear as localized "droplets" of the erosion/deposition process and thus look essentially different from the segregation fingers reported on a rough substrate [16]. Note that their shape is reminiscent of many natural patterns obtained in debris or mud flows [17] displaying well-defined widths at the values of about hundreds of a typical rock size.

The experimental findings were put to test in the context of a phase-field model developed for the description of dense granular flows. At a qualitative level the agreement between theory and experiments is impressive. (i) Existence of steady-state solitary avalanches propagating downhill with a shape similar to experiment. (ii) Generic zero wave number (long-wave) transverse instability compatible with the experimental divergence of the selected wavelength close to the instability threshold. Far from the threshold, linear growth rate dependence with the modulation wavenumber q compatible with measurements. (iii) Coarsening in the later evolution of the instability. (iv) Fingering instability with localized droplet-like avalanches (also similar to those described in [11]). The analysis predicts that the transverse instability ceases to exist when the rescaled transport coefficient α decreases (see Fig. 8). However, the model does not provide explicit expression for α due to the dependence of granular viscosity ν on other external parameters (e.g. local pressure, see [9,10]). Rough estimates of α can be extracted from the flow rules in Ref. [6] which gives the relation between depth-average velocity $\langle V \rangle$ and height h: $\langle V \rangle / \sqrt{hg} \approx \bar{\beta} h / h_{\text{stop}}(\theta) + const$, where dimensionless material constant $\bar{\beta} \approx 1$ for sand and $\bar{\beta} \approx 0.2$ for glass beads. Since flux of grains $J = h\langle V \rangle \approx \bar{\beta}\sqrt{g}h^{5/2}/h_{\text{stop}}(\theta)$, to compare with flux expression in

Eq. (3), we write for the fully-fluidized state ($A \approx 1$): $J \approx \bar{\beta}\sqrt{g}h^3/h_{stop}^{3/2}(\theta)$. Since the typical time in the problem τ_ρ is of the order collision time $\sqrt{d/g}$, after rescaling $x \to x/d$, $h \to h/d$, $t \to t/\tau_\rho$, we obtain in the dimensionless form the estimate for $\alpha \approx \bar{\beta}(d/h_{stop}(\theta))^{3/2}$. Since $h_{stop} \to \infty$ with the decrease of the angle θ, the instability should disappear for smaller angles, which is verified experimentally. The analysis also predicts that the instability could be suppressed for the case of small rheological parameter $\bar{\beta}$ corresponding to smooth glass beads. Thus, the model provides a crucial prediction on the transverse instability mechanism which lies in the dependence of the solitary wave velocity on the flowing mass trapped in the avalanche. This result is recovered experimentally. Still, important issue remains on how to bring more quantitative comparison between the theory and the experimental measurements.

References

1. Iverson, R.M.: Rev. Geophys. **35**, 245–296 (1997)
2. Hampton, M.A., Lee, H.J., Locat, J.: Rev. Geophys. **34**, 33–59 (1996)
3. Bouchaud, J.-P., Cates, M., Prakash, J.R., Edwards, S.F.: J. Phys. Fr. I **4**, 1383 (1994)
4. Aradian, A., Raphaël, E., de Gennes, P.-G.: C. R. Phys. **3**, 187 (2002)
5. Pouliquen, O.: Phys. Fluids **11**, 542 and 1956 (1999)
6. Midi G.D.R. (collective work): Eur. Phys. J. E **14**, 341 (2004)
7. Pouliquen, O., et al.: Powders & Grains 2005, p. 850. In: Garcia-Rojo, R., Herrmann, H.J., McNamaca, S. (eds.) Balkema, Rotterdam
8. Daerr, A., Douady, S.: Nature **399**, 241 (1999)
9. Aranson, I.S., Tsimring, L.S.: Phys. Rev. E **64**, 020301 (2001)
10. Aranson, I.S., Tsimring, L.S.: Phys. Rev. E **65**, 061303 (2002)
11. Borzsonyi, T., Halsey, T.C., Ecke, R.E.: Phys. Rev. Lett. **94**, 208001 (2005)
12. Malloggi, F., Lanuza, J., Andreotti, B., Clément, E.: Powders & Grains, p. 997. In: Garcia-Rojo, R., Herrmann, H.J., McNamaca, S. (eds.) Balkema Rotterdam (2005)
13. Malloggi, F., Lanuza, J., Andreotti, B., Clément, E.: Europhys. Lett. **75**, 825 (2006)
14. Aranson, I.S., Malloggi, F., Clément, E.: Phys. Rev. E **73**, 050302 (2006)
15. Pouliquen, O., Valance, J.W.: Chaos **9**, 621 (1999)
16. Pouliquen, O., Delour, J., Savage, S.B.: Nature **386**, 816 (1997)
17. Felix, G., Thomas, N.: Earth Planet. Sci. Lett. **221**, 197 (2004)
18. Aranson, I.S., Tsimring, L.S.: Rev. Mod. Phys. **78**, 641 (2006)
19. Volfson, D., Tsimring, L.S., Aranson, I.S.: Phys. Rev. E **68**, 021301 (2003)
20. Daerr, A.: Phys. Fluids **143**, 2115 (2001)
21. Daerr, A., Lee, P., Lanuza, J., Clément, E.: Phys. Rev. E, **67**, 065201 (2003)